AGU ADVANCING EARTH AND SPACE SCIENCE

Geophysical Research Letters®

RESEARCH LETTER
10.1029/2022GL098872

Broadband Dynamic Rupture Modeling With Fractal Fault Roughness, Frictional Heterogeneity, Viscoelasticity and Topography: The 2016 M_w 6.2 Amatrice, Italy Earthquake

T. Taufiqurrahman[1], A.-A. Gabriel[1,2], T. Ulrich[1], L. Valentová[3,4], and F. Gallovič[3]

[1]Department of Earth and Environmental Sciences, Ludwig-Maximilians-Universität München, Munich, Germany, [2]Scripps Institution of Oceanography, UC San Diego, La Jolla, CA, USA, [3]Department of Geophysics, Faculty of Mathematics and Physics, Charles University, Prague, Czech Republic, [4]Instituto Nazionale di Geofisica e Vulcanologia, Milan, Italy

Key Points:

- We propose a novel approach to design data-driven, 3D physics-based broadband dynamic rupture scenarios from low-resolution models
- Our synthetics fit observations in terms of velocity and accelerations waveforms, as well as Fourier-amplitude-spectra up to ~5 Hz
- Analyzing the role of earthquake modeling ingredients highlights the importance of dynamic source heterogeneity for broadband ground-motion

Supporting Information:

Supporting Information may be found in the online version of this article.

Correspondence to:

A.-A. Gabriel,
algabriel@ucsd.edu

Citation:

Taufiqurrahman, T., Gabriel, A.-A., Ulrich, T., Valentová, L., & Gallovič, F. (2022). Broadband dynamic rupture modeling with fractal fault roughness, frictional heterogeneity, viscoelasticity and topography: The 2016 M_w 6.2 Amatrice, Italy earthquake. *Geophysical Research Letters*, *49*, e2022GL098872. https://doi.org/10.1029/2022GL098872

Received 27 MAR 2022
Accepted 9 NOV 2022

Abstract Advances in physics-based earthquake simulations, utilizing high-performance computing, have been exploited to better understand the generation and characteristics of the high-frequency seismic wavefield. However, direct comparison to ground motion observations of a specific earthquake is challenging. We here propose a new approach to simulate data-fused broadband ground motion synthetics using 3D dynamic rupture modeling of the 2016 M_w 6.2 Amatrice, Italy earthquake. We augment a smooth, best-fitting model from Bayesian dynamic rupture source inversion of strong-motion data (<1 Hz) with fractal fault roughness, frictional heterogeneities, viscoelastic attenuation, and topography. The required consistency to match long periods allows us to quantify the role of small-scale dynamic source heterogeneities, such as the 3D roughness drag, from observational broadband seismic waveforms. We demonstrate that 3D data-constrained fully dynamic rupture synthetics show good agreement with various observed ground-motion metrics up to ~5 Hz and are an important avenue toward non-ergodic, physics-based seismic hazard assessment.

Plain Language Summary Models of earthquakes are used to better understand the origin and features of strong seismic shaking using supercomputers. But the connection of such computer simulations with actual measurements is complex. This study suggests a new way to use observations, computer models, and physics to model details of the damaging ground shaking recorded during the 2016 Amatrice, Italy, earthquake. We start from an earlier, relatively low-resolution earthquake model that matches seismograms at low frequencies (<0.5–1 Hz), derived using many Monte Carlo simulations. We carefully enhance this earthquake model by adding roughness to the slipping fault, smaller-scale variations of the frictional resistance of this fault to earthquake slip, mountains and basins scattering the seismic waves, and the effects of anelastic damping of wave amplitudes while they propagate. We show that we now also match the seismic waves at frequencies up to 5 Hz, while not losing the good match at long periods. This result is important to better understand how hazardous earthquakes in specific regions may be. Our modeling indicates which ingredients are required in computer simulations to generate realistic ground motions for physics-based seismic hazard assessment.

1. Introduction

Simulations of broadband (>1 Hz) ground motions are of great importance to seismologists and the earthquake engineering community. Even though we often lack detailed knowledge of the subsurface and earthquake source processes at small scales, it is essential to understand the generation and characteristics of the high-frequency seismic wavefield coinciding with most buildings' resonance frequencies. Broadband ground motions have been successfully simulated using hybrid techniques (e.g., Graves & Pitarka, 2010; Mai et al., 2010; Sommerville et al., 1999) that combine low-frequency deterministic ground motion synthetics with stochastically generated high-frequency components. While classical kinematic approaches are tremendously useful specifically for seismic hazard assessment and engineering, they do not guarantee a physically consistent source description and do not permit data-driven inferences on the fundamentals of how faults slip co-seismically, specifically on smaller scales (Burjánek & Zahradník, 2007; Mai et al., 2016; Tinti et al., 2005). Dynamic rupture models provide mechanically viable correlations among macroscopic earthquake rupture parameters, such as slip rate and rupture time, rooted in laboratory-derived friction laws and elastodynamics (Guatteri et al., 2004; Savran & Olsen, 2020; Schmedes et al., 2010). Nevertheless, mainly due to the associated computational demands at high frequencies, fully dynamic rupture scenarios have rarely been validated against real seismograms in a broad frequency range.

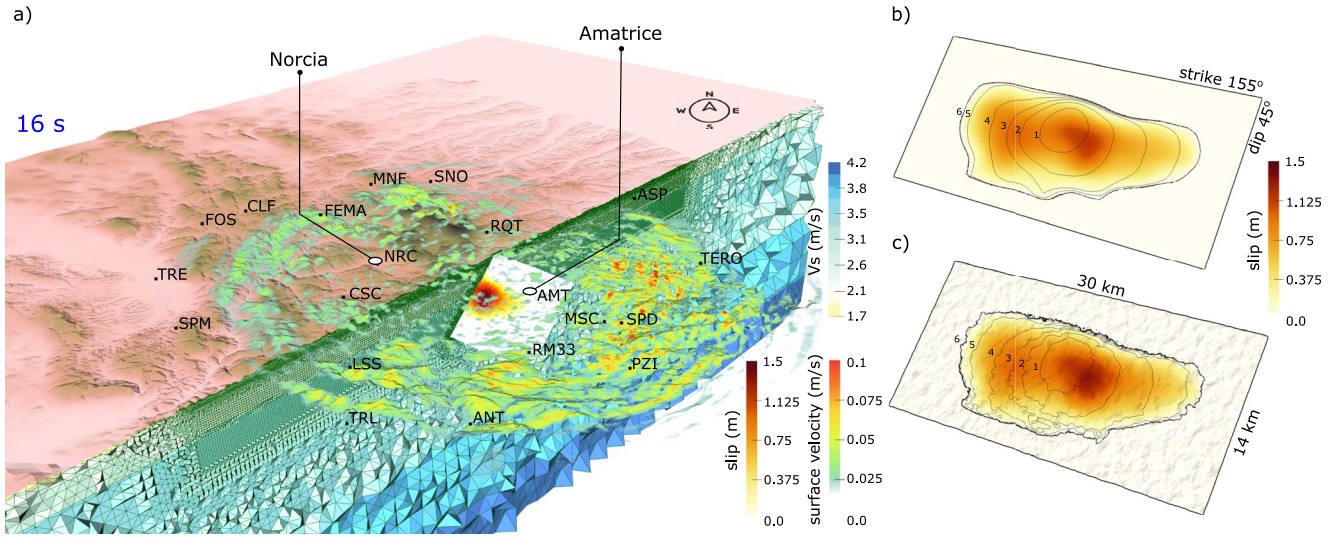

Figure 1. (a) Three-dimensional dynamic rupture model setup of the 2016 M_w 6.2 Amatrice, Central Italy, earthquake. Snapshot of the absolute surface velocity at a simulation time of 16 s. The model is discretized by an unstructured tetrahedral mesh refined in the vicinity of the fault and the high-resolution topography. Twenty strong-motion stations used in this study are marked in black (see Table S1 in Supporting Information S1). Mesh elements are colored by shear wave velocity (V_s). (b, c) Fault slip for the smooth Bayesian dynamic source inversion reference model (b) and the broadband dynamic rupture model (c). Black curves represent rupture front contours every 1 s.

Hybrid synthetic waveforms lack deterministic information at higher frequencies and pose challenges in the realistic parameterization of wave propagation and earthquake rupture. Indeed, high-frequency radiation may arise, for instance, from acceleration and deceleration of the rupture front (Madariaga, 1977) caused by fault kinks, segmentation, or roughness (e.g., Bydlon & Dunham, 2015; Shi & Day, 2013), frictional or stress heterogeneities (e.g., Ripperger et al., 2008; Valentová et al., 2021) or from off-fault damage (e.g., Okubo et al., 2019; Yamashita, 2000). Additionally, the radiated wavefield is scattered by complex topography and structural heterogeneities (e.g., Hartzell et al., 2016; Imperatori & Mai, 2013; Pitarka et al., 2021; Takemura et al., 2015).

Recent advances in high-performance computing allow deterministic 3D regional-scale broadband simulations to resolve frequencies up to 10 Hz (e.g., Heinecke et al., 2014; Pitarka et al., 2021; Rodgers et al., 2020; Savran & Olsen, 2020). Such simulations often assume a kinematic, thus predefined, finite earthquake source representation. In distinction, dynamic rupture models offer physically self-consistent descriptions of the earthquake rupture process. Generic dynamic rupture simulations across rough faults (both in 2D or 3D, e.g., Bruhat et al., 2020; Bydlon & Dunham, 2015; Dunham et al., 2011; Shi & Day, 2013; Withers et al., 2018) are characterized by highly complex rupture processes translating into ground motion synthetics that can match empirical ground-motion prediction equations (GMPEs).

The 24 August 2016, M_w 6.2 Amatrice earthquake (Chiaraluce et al., 2017; Michele et al., 2020) is the first in the Amatrice-Visso-Norcia earthquake sequence in the Central-Northern Apennine system of NW-SE aligned normal faults. It was the sequence's most destructive event, causing extensive damage to surrounding buildings and infrastructure (Michele et al., 2016). The earthquake was recorded by a remarkably dense network of strong ground motion instruments, including 20 near-source stations within a radius of 50 km from the earthquake epicenter (Figure 1, Table S1 in Supporting Information S1). The two closest stations, in Amatrice (AMT) and Norcia (NRC), are located only a few kilometers away from the fault.

The source process of the Amatrice event has been imaged using seismic data (Pizzi et al., 2017; Tinti et al., 2016), geodetic data (e.g., Cheloni et al., 2017; Walters et al., 2018), or both (Cirella et al., 2018; Kheirdast et al., 2021), suggesting pronounced source heterogeneities. However, kinematic finite-fault inversions are challenged by inherent non-uniqueness (Gallovič & Ampuero, 2015; Mai et al., 2016; Ragon et al., 2018; Shimizu et al., 2020; Tinti et al., 2021). Dynamic source inversions recovering friction parameters and the initial state of fault stress offer a data-driven source description compatible with earthquake physics (e.g., Peyrat & Olsen, 2004) but require a sufficiently simple dynamic rupture model to reduce the computational cost of the forward problem. A Bayesian dynamic inversion using the Parallel Tempering Monte Carlo algorithm (Gallovič et al., 2019a; Sambridge, 2013)

was applied to the Amatrice earthquake, utilizing band-pass filtered (between 0.05 and 0.5–1 Hz) strong ground motion data by Gallovič et al. (2019b). Assuming a 1D medium with planar topography, the best-fitting model was used to predict ground motions up to higher frequencies than considered in the inversion (up to ∼5 Hz). Yet this approach poorly matched the high-frequency content, presumably most sensitive to unresolvable small-scale features of the rupture process.

We here propose a new approach to simulate data-fused broadband ground motion synthetics using 3D dynamic rupture modeling. Our starting point is the best-fitting model from the Bayesian dynamic source inversion of the Amatrice earthquake (Figure 1b, hereafter named "reference model"). We self-consistently augment this smooth reference model by adding fault roughness, small-scale frictional heterogeneities, viscoelastic attenuation, and topography yielding realistic high-frequency radiation without disrupting the large-scale characteristics of the reference model. The synthetic near-field ground motions show good agreement with various observed ground-motion metrics up to frequencies of ∼5 Hz.

2. Ingredients for Broadband Dynamic Rupture Modeling

While a wide range of mechanisms may enhance high-frequency radiation, the here selected processes have been proposed to be first-order relevant (Bruhat et al., 2020; Fang & Dunham, 2013; Pitarka et al., 2021; Shi & Day, 2013; Takemura et al., 2015; Withers et al., 2018) and are reasonably well constrained beyond the case of the Amatrice earthquake. For example, Bydlon and Dunham (2015) find that fault roughness, and not material heterogeneity, dominates the dynamic rupture process. Ma et al. (2008) discuss that large-scale topography can have locally stronger effects on modeled ground motions than 3D subsurface structure. Contrary to the latter, the topography is typically well-constrained by observations and readily available in high resolution. Viscoelastic attenuation is important to capture the decay of seismic energy with increasing propagation distance (e.g., Hu et al., 2022; Wollherr et al., 2019). Computational advances (e.g., Heinecke et al., 2014; Premus et al., 2020) now allow us to show in fully dynamic rupture models of a real earthquake that fault roughness, frictional heterogeneity, topography, and attenuation have complementary effects. Dynamic rupture source complexity enhances high-frequency generation, while topography effects elongate the synthetic coda signals, together yielding more realistic ground motions.

We build our model upon Bayesian dynamic rupture inversion of the 2016 Amatrice earthquake following the approach of Gallovič et al. (2019b) with the improved forward solver FD3D_TSN (Premus et al., 2020), which was verified in a suite of dynamic rupture benchmarks (Harris et al., 2018). The inversion is performed for a 30 km long and 14 km wide planar fault governed by a slip-weakening friction law (Ida, 1972; Palmer et al., 1973). The dynamic rupture slip rate functions along the fault are convolved with pre-calculated Green's functions representing impulse responses of the medium. In this step, the fault is dipping at 45°, embedded in the 1D velocity structure of Ameri et al. (2012) with a flat free surface. The dynamic models are characterized by three spatially heterogeneous parameters: (a) the initial shear stress along dip τ_i, (b) the friction drop, μ_s-μ_d, with μ_s and μ_d the static and dynamic friction coefficient respectively, and (c) the slip-weakening distance D_c. Yielding occurs when the shear stress τ reaches the fault strength $\tau_s = \mu_s\sigma_n$, where σ_n is assumed as linearly depth-dependent normal stress with a gradient of 8.52 MPa/km and a minimum value of 0.1 MPa. The initial along-strike shear stress $\tau_{strike0}$ is assumed to be zero. The dynamic friction coefficient μ_d is fixed to 0.4, and frictional cohesion of 0.5 MPa is assumed everywhere on the fault. The best-fitting model from the Bayesian inversion represents the reference model of this study. We then perform high-resolution enhanced 3D dynamic rupture simulations using the open-source software package SeisSol (https://github.com/SeisSol/SeisSol), resolving seismic wavefield up to 5 Hz (locally up to 10 Hz) within 50 km distance of the fault using an unstructured, statically adaptive mesh consisting of 80 million tetrahedral elements (Figure 1a, Text S1 in Supporting Information S1).

2.1. Fault Roughness

The reference model's dynamic parameters are first bilinearly interpolated from their 1.75 km along-dip and 2.3 km along-strike reference resolution into a denser 25 m sampled grid (see Figure 2, column a). Next, we adapt the fault morphology to adhere to a band-limited self-similar (Hurst exponent $H = 1$) fractal surface. The amplitude-to-wavelength ratio α of natural faults ranges between 10^{-4} and 10^{-2} (Power & Tullis, 1991), and we here use $\alpha = 10^{-2}$ allowing direct comparability to earlier studies (Bruhat et al., 2020; Fang & Dunham, 2013;

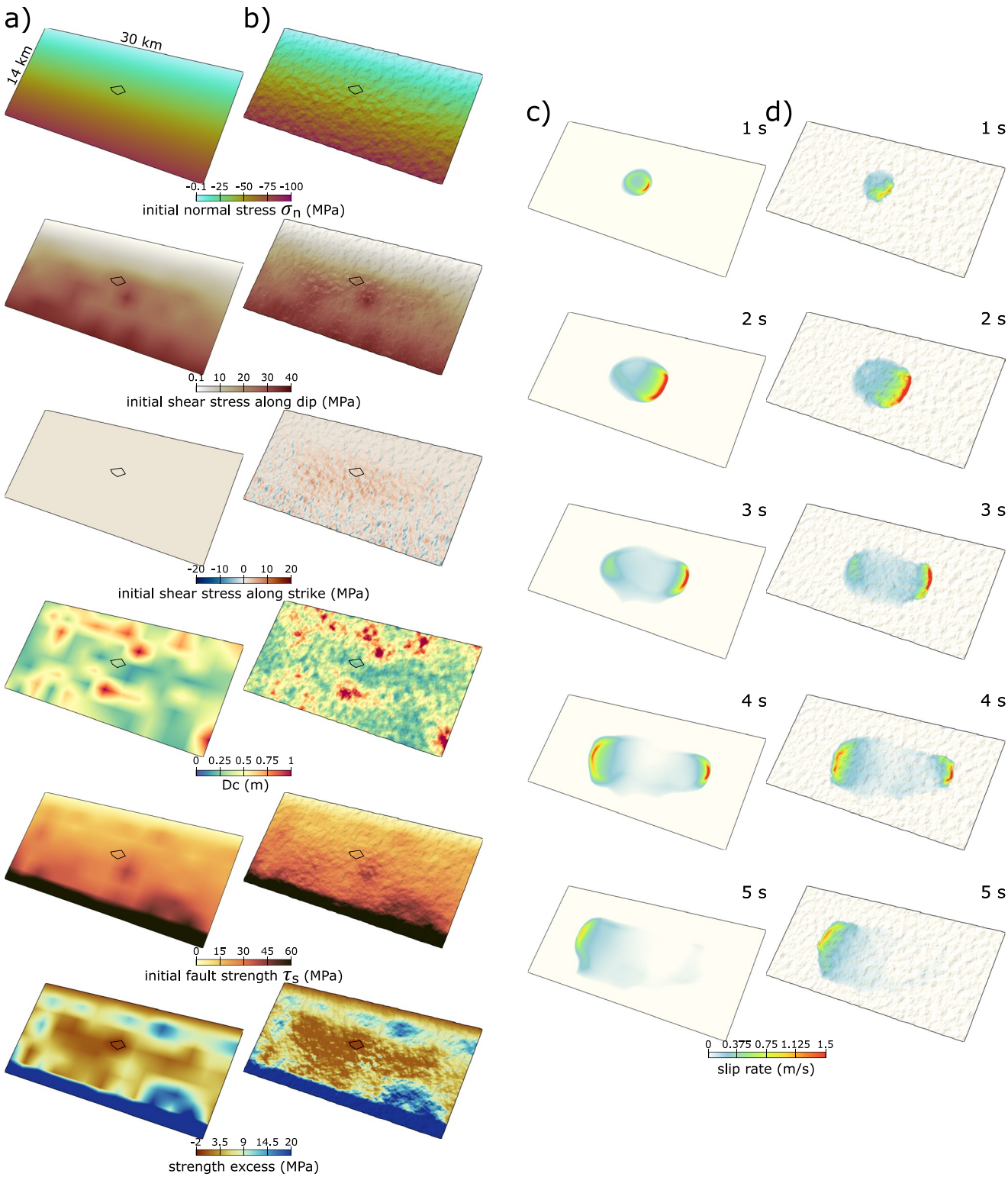

Figure 2. (a, b) Comparison of dynamic parameters used in the reference model (a), and the broadband rough fault model (b). Fractal heterogeneity is also added to the distribution of slip weakening distance (D_c). The black contour marks the nucleating negative strength excess area. (c, d) Dynamic rupture propagation in the reference (c) and broadband (d) rough fault models of the Amatrice earthquake. Snapshots of the absolute fault slip rates illustrate the similar space-time evolution in both models.

Shi & Day, 2013; Withers et al., 2018). This nearly upper limit of roughness may be related to the presumably immature fault system hosting the Amatrice earthquake (Pizzi et al., 2017), as suggested from regional slow long-term slip rates (Galadini and Galli, 2003), the young age of post-orogenic extension in the Apennines and the decoupling effect of multiple décollement levels and strong rheological contrasts (e.g., Ascione et al., 2013; Tondi et al., 2020).

The fractal surface wavelengths are band-limited between λ_{min} and λ_{max}. Choosing $\lambda_{min} = 200$ m balances resolution requirements and computational cost for our setup and aligns with previous 3D fault roughness studies (Fang & Dunham, 2013; Shi & Day, 2013). Our choice of $\lambda_{max} = 2$ km is motivated by the ~2 km spatial resolution of the dynamic parameters in the reference model.

2.2. 3D Roughness Drag and Heterogeneous Initial Stresses

Shear and normal stresses are dynamically perturbed by fault roughness during rupture propagation. The general scaling of the "roughness drag" (Dunham et al., 2011), an additional shear resistance to slip, was derived for a 1D rough fault in a 2D quasi-static boundary perturbation analysis by Fang and Dunham (2013) as

$$\tau_{drag}{}^{2D} = 8\,\pi^3\alpha^2\,G^*\Delta(1/\lambda_{min} - 1/\lambda_{max}) \approx 8\,\pi^3\alpha^2\,G^*\Delta/\lambda_{min}, \quad (1)$$

with Δ being the fault slip, λ_{min} the minimum roughness wavelength, and $G^* = G/(1-\nu)$, where G and ν are shear modulus and Poisson's ratio, respectively, and $\lambda_{max} >> \lambda_{min}$.

To preserve the overall characteristics of the reference scenario while incorporating fault roughness, we must compensate the roughness drag in the initial loading by increasing the reference initial shear tractions as $\tau_{dip} = \tau_{dip0} + \tau_{drag}{}^{3D}$ and $\tau_{strike} = \tau_{strike0} + \tau_{drag}{}^{3D}$. We numerically approximate the roughness drag (following Dunham et al., 2011, but for the first time based on 3D dynamic rupture models) as

$$\tau_{drag}{}^{3D} = C\,\tau_{drag}{}^{2D}, \quad (2)$$

where C is a dimensionless coefficient. In Text S2 in Supporting Information S1, we demonstrate in numerical experiments that C can be approximated from $\tau_{drag}{}^{2D}$ using characteristics of the reference model slip distribution. For our choice of $n = 4$ elements to resolve $\lambda_{min} = 200$ m, we obtain C of ~0.44. The average value of $\tau_{drag}{}^{3D}$ across the rupture area is ~1.4 MPa. Our lower $\tau_{drag}{}^{3D}$ is intuitive since the material off a 3D roughness feature can also deform perpendicular to slip in distinction to the 2D case. We caution that while $\tau_{drag}{}^{2D}$ is defined for 2D in-plane quasi-static rupture, proper analytical treatment of the 3D (dynamic) roughness drag is very complex. The formulation of the roughness drag is based on stationary statistics and thus applies in the slipping (or slipped) region well behind the rupture front, challenging analytical extensions to account for rupture front curvature, inertia, or slip gradients in the vicinity of the rupture front. This motivates our empirical approach (see also Text S2 in Supporting Information S1). We account for the 3D roughness drag while preserving the smooth reference initial stress distribution by loading the rough fault with a heterogeneous regional stress tensor: we first adapt the smooth reference initial fault loading to balance roughness drag, then expose the now rough fault to the adapted loading (Text S3 in Supporting Information S1). As a result, the broadband model features roughness-induced small-scale fluctuations of the initial shear and normal tractions (Figure 2b), consisting of both releasing and restraining slopes that bring the fault closer and farther from failure, respectively (Figure S2 in Supporting Information S1).

2.3. Frictional Heterogeneity

We perturb the smooth variation of the reference characteristic frictional slip weakening distance $D_c{}^0$, the spatially most variable dynamic parameter in the reference Bayesian dynamic inversion. The relative standard deviation of D_c is on the order of 50% (Gallovič et al., 2019b), highlighting its importance as a proxy for unaccounted geometrical and geological features. We use a band-limited fractal distribution. We prescribe $D_c = \max(0.14\text{ m}, D_c{}^0(1+\varepsilon))$, where 0.14 m is the minimum value of $D_c{}^0$, and ε follows a fractal distribution of amplitude-to-wavelength ratio $\alpha = 10^{-2}$ generated from a different random seed than the one used for the fault roughness. Including small-scale heterogeneous D_c in our broadband model is a proxy for frictional or stress asperities that have been shown to be important for high-frequency radiation in previous work (e.g., Galvez

et al., 2020; Ripperger et al., 2008). Heterogeneous D_c contributes to radiating additional energy due to fault-local acceleration and deceleration.

2.4. Topography and Viscoelasticity

In our broadband dynamic rupture, the flat free surface used in the inversion is superseded by high-resolution topography data sampled to 150 m resolution (Farr et al., 2007). The modeled 3D domain spans 300 × 300 km horizontally and extends to a depth of 150 km to avoid any undesired reflections from the (imperfectly) absorbing boundaries. We incorporate the 1D velocity model, with $V_p = 1.86V_s$, and viscoelastic attenuation, with $Q_p = 2Q_s$, inferred by Ameri et al. (2012), see Table S2 in Supporting Information S1. Accounting for topography and viscoelasticity is complementary to including dynamic source heterogeneity. Realistic 3D topography scattering redistributes seismic energy to later arrival times enhancing synthetic seismogram coda signals, an effect that cannot be obtained when considering source complexity only.

3. Broadband Rupture Dynamics and Ground-Motion Validation

3.1. Rupture Dynamics

We compare the broadband dynamic rupture model, incorporating fault roughness, small-scale D_c variation, and topography to the reference model with a planar fault, a flat free surface, and smoothly varying initial conditions, in terms of fault slip (Figures 1b and 1c), slip rate space-time evolution (Figures 2c and 2d), and moment rate release (Figure S3 in Supporting Information S1).

Figures 1b and 1c and Figures 2c and 2d demonstrate similar large-scale slip evolution. The seismic moment of the broadband model is 2.8×10^{18} Nm, corresponding to $M_w = 6.24$, which is comparable to the reference model with 2.6×10^{18} Nm seismic moment ($M_w = 6.20$). We highlight that both models recover the remarkably weak and slow nucleation phase (Gallovič et al., 2019b; Tinti et al., 2016), as was also inferred for the Norcia earthquake (Tinti et al., 2021). The nucleation is followed by bilateral rupture, which is slower toward the NW than toward the SE in both models. At smaller scales, the broadband model features decoherence of rupture fronts (Shi & Day, 2013). Locally fluctuating rupture speeds are due to acceleration and deceleration at releasing and restraining slopes, heterogeneous initial shear and normal traction, and D_c heterogeneity. Peak slip rates are increased by ∼15% in the broadband model, while both models feature pulse-like ruptures, and rise time remains largely unaffected.

Comparisons of moment rate releases (Figure S3a in Supporting Information S1), moment rate spectra (Figure S3b in Supporting Information S1), and the second time-derivative of moment rate releases (Figure S3c in Supporting Information S1) illustrate the effects of the fault roughness, heterogeneous loading, and D_c on the high-frequency rupture radiation. While the two distinct episodes of moment rate release are well recovered, its first peak is about 20% higher in the broadband model than the reference model (Figure S3a in Supporting Information S1), reflecting the increase in negative strength excess in the nucleation region required for broadband self-sustained spontaneous dynamic rupture across the rough, frictionally heterogeneous fault.

3.2. Ground Motions

Figure 3 compares the observed three-component velocity and acceleration waveforms recorded at the 20 strong-motion stations (Figure 1, Luzi et al., 2016) with synthetics from the broadband dynamic rupture model. The overall agreement in terms of waveform shape and duration is good for both velocity and acceleration waveforms. The synthetic amplitudes fit velocity recordings very well at most stations (Figure 3a). Nevertheless, the modeled acceleration amplitudes are significantly underestimating some station components (Figure 3b, e.g., NRC, MNF, FOS, ASP). Analogous plots for the reference model and the rough, heterogeneous fault model without topography are shown in Figures S4 and S5 in Supporting Information S1, respectively. We isolate the effect of using small-scale heterogeneous D_c in comparison to the smoothly varying D_c from Gallovič et al. (2019b) in Figures S3 (moment rates) and Figure S6 (synthetics) in Supporting Information S1.

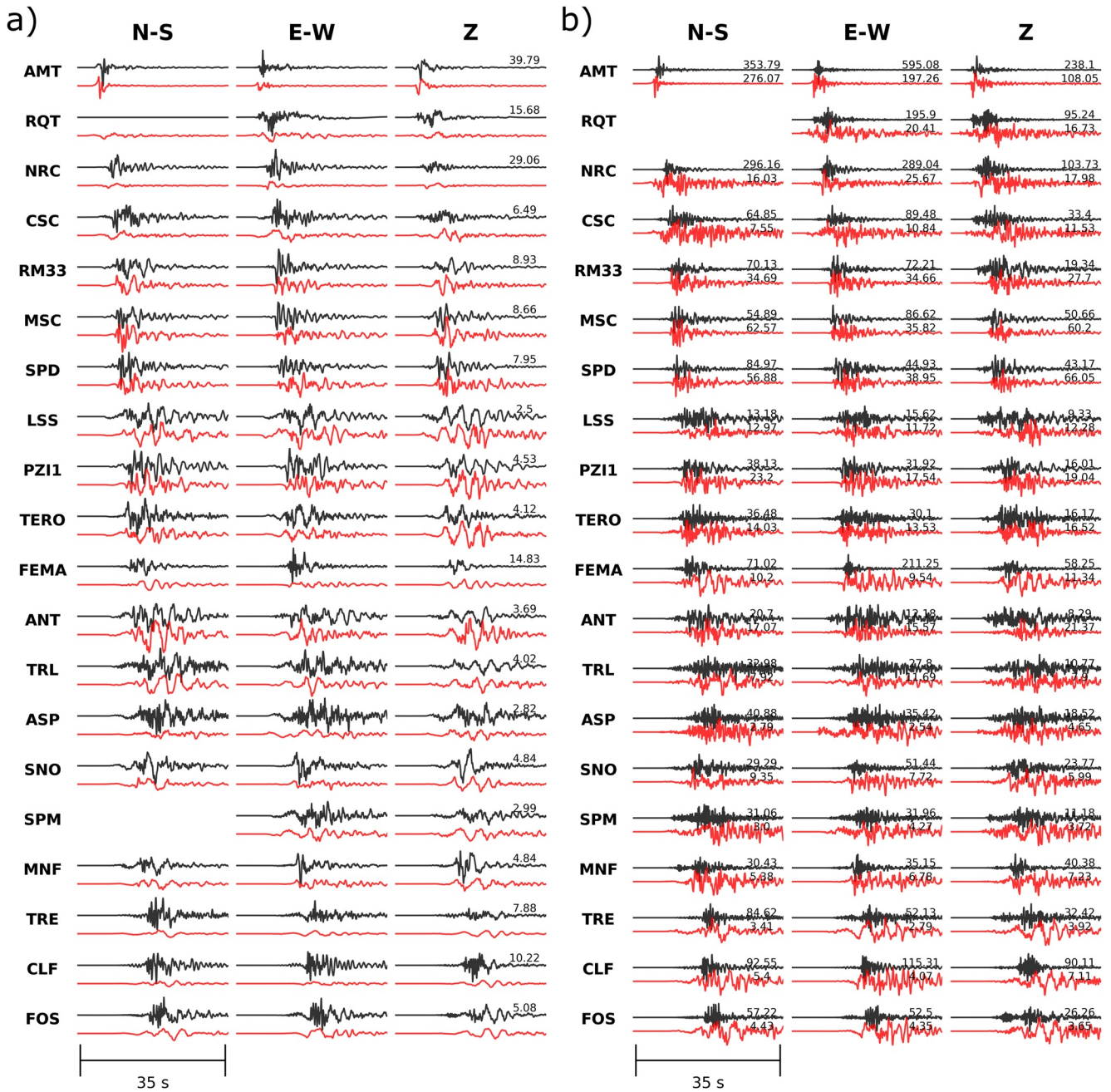

Figure 3. Comparison of observed (black) and simulated (red) components (NS, EW, and Z) of (a) ground velocity (in cm/s) and (b) acceleration (in cm/s^2) band-pass filtered between 0.05 and 5 Hz for all 20 stations (Figure 1), ordered by epicentral distance. Synthetics are from the broadband dynamic rupture scenario incorporating fault roughness, D_c heterogeneity, and topography. Both observed and synthetic waveforms are scaled by their maximum value, which is indicated on the right-hand side of each plot. Velocity waveforms are scaled by the maximum value of the observed records at each station, while acceleration waveforms are scaled component-wise.

To highlight the role of the fault roughness, frictional heterogeneity, and topography, Figure 4 compares observed EW velocity and acceleration waveforms and Fourier Amplitude Spectra (FAS) with synthetics of three models: the reference, the broadband rough fault model with topography, and the broadband rough fault model without topography. All components and stations are shown in Figures S7–S13 in Supporting Information S1. The synthetic waveforms of the broadband models match long-period data (0.05–0.5 Hz) equally well as the reference model. Nevertheless, the reference model provides waveforms clearly depleted at high frequencies. A general trend is that fault roughness and topography enhance and elongate waveforms at high frequencies, respectively, although not to the same extent at all stations. The increase in high-frequency content in the broadband waveforms

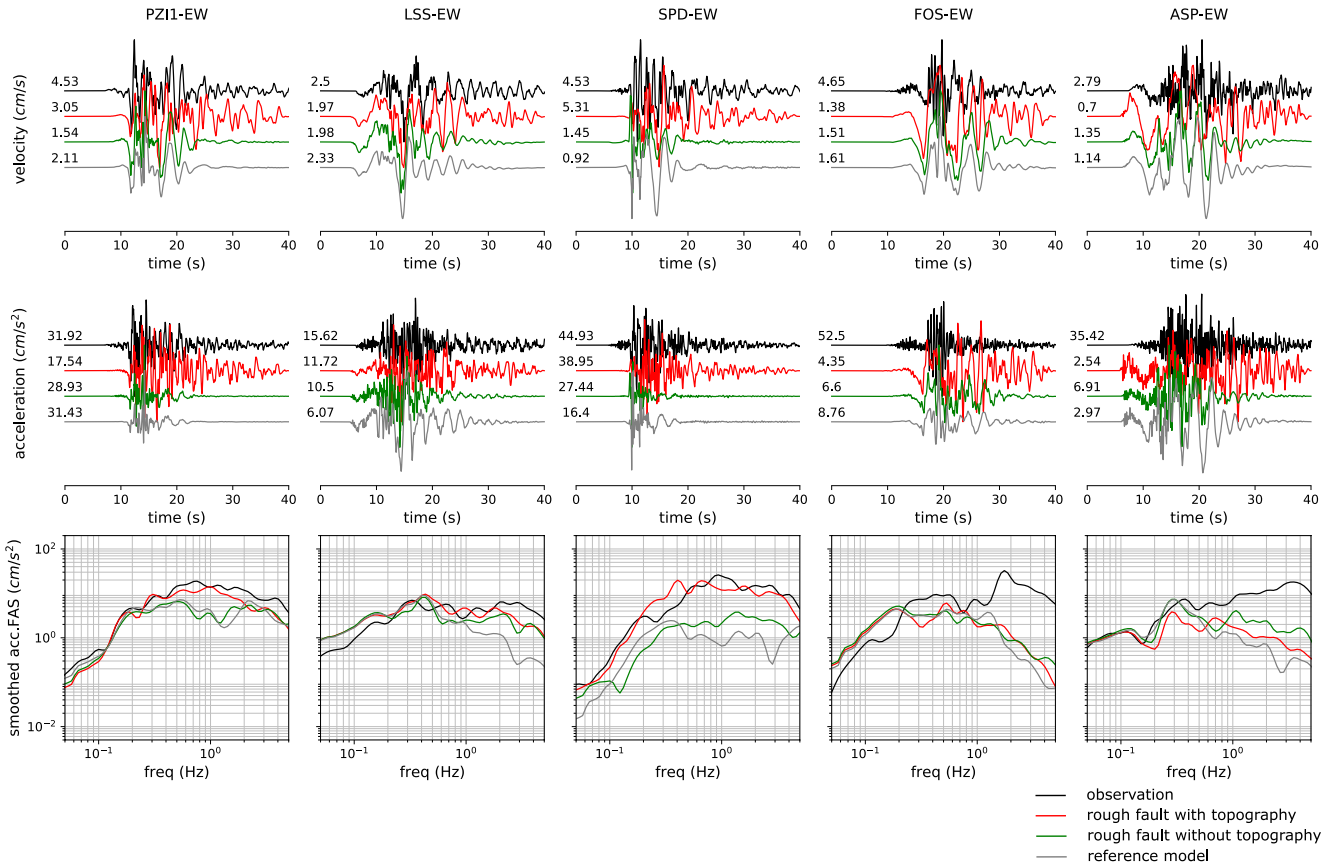

Figure 4. Comparison of EW component of broadband synthetic ground-velocity (top) and acceleration (middle) waveforms from the broadband rough fault model with topography (red), the broadband rough fault model without topography (green), and the reference model (gray) compared with observations (black) at five selected stations (see Figure 1). All waveforms are scaled by their maximum values, indicated on the left-hand side of each trace. (bottom) Smoothed Fourier amplitude spectra of the acceleration waveforms using the method of Konno and Ohmachi (1998). The observed data are tapered with a 35 s cosine window.

without topography (green) is clearly limited in duration compared to the same model incorporating topography (red). High-frequency ground motions are amplified early-on by fault roughness, while topography-induced scattered waves prolong their duration. The combination of both effects is most pronounced in the central and SE part of the hanging wall region (see, e.g., stations PZI1, LSS, and SPD in Figure 4 and Figure S8 in Supporting Information S1, or MSC, AMT, and ANT in Figures S7, S10, S11, and S13 in Supporting Information S1). At some stations (e.g., stations FOS and ASP), our broadband synthetic spectra are improved yet underestimate the observed spectra at frequencies higher than 1 Hz. We may speculate that larger station-source distances, as for FOS and ASP, and local subsurface complexity such as basin edge effects render more realistic 3D velocity models than used here, important for physics-based broadband modeling. Similarly, fully considering site effects may amplify high-frequency waveform spectra.

Animations of the three components of the velocity wavefield for the reference and broadband models are shown in Movies S2–S7 in Supporting Information S1. They illustrate how seismic waves are both reflected and scattered upon propagating across sharp topographical features like mountains and hills, which explains the prolonged duration of the seismic signal for several receivers (e.g., stations LSS and SPD, Figure 4). Although viscoelastic attenuation is generally important to capture the decay of seismic energy during topography scattering, a comparison between our models with and without attenuation in Figure S14 in Supporting Information S1 shows relatively minor effects (e.g., for stations SPD, PZI1, TERO).

Figures S15 and S16 in Supporting Information S1 quantify the fit of the synthetic ground motions of the broadband and reference models with observations using Goodness-of-fit (GOF) metrics (Olsen & Mayhew, 2010), including peak ground velocity and displacement, spectral acceleration, FAS, energy duration, and cumulative energy (Text S4 in Supporting Information S1). The broadband model with topography fits the observations

better (GOF 45–65) than the reference model (GOF 35–55) and the broadband model without topography (GOF 40–60).

Figure S17 in Supporting Information S1 details the model bias and standard deviation over the 0.5–10 s period range, averaged over 20 stations used in this study. In general, a near-zero model bias over a specific period suggests that simulated ground motions match observations reasonably well at given frequencies. The reference model fits the observations only at periods longer than 2 s. Compared to the reference model, the fit of the broadband model without topography (Figure S17b in Supporting Information S1) is improved (30%–40% lower bias) at periods shorter than 2 s. The broadband model with topography shows an even better fit (40%–50% lower bias than the reference model, Figure S17c in Supporting Information S1). However, while both broadband models preserve a perfect fit at periods longer than 2 s, some synthetics still underestimate the observations at periods shorter than 2 s, as discussed above."

4. Discussion

Recorded broadband ground motions are widely used in earthquake engineering to inform the performance-based design of structures. Typically, generic strong-motion waveforms that fit specific ground motion metrics are selected from a strong-motion database for that purpose (Iervolino et al., 2010). Also, probabilistic seismic hazard analyses often rely on such so-called ergodic ground-motion models (GMMs, e.g., Petersen et al., 2019). Yet, these may not reflect the conditions of a specific region of interest. Regional synthetic broadband ground motions from 3D dynamic rupture inversions, which offer a physically consistent representation of earthquakes, can sample conditions that are not sufficiently constrained in empirical models toward the development of non-ergodic, physics-based GMMs (Frankel et al., 2018; Graves et al., 2011; Moschetti et al., 2017; Wirth et al., 2018; Withers et al., 2020). Our proposed broadband dynamic rupture models can be extended to account for other distinctive regional characteristics, such as a listric or segmented fault geometry, 3D velocity models including low velocity layers and basins, and fault zone plasticity (Roten et al., 2014). They may also inform PSHA-targeted kinematic rupture generators while inherently ensuring realistic scaling of earthquake characteristics (e.g., Savran & Olsen, 2020). Our models emphasize the need to include (a) small-scale source characteristics to enhance the high-frequency source radiation during the rupture propagation, and (b) topography to increase the duration due to scattering. The duration of the latter effect is controlled by viscoelastic attenuation.

We carefully analyze the effects of adding roughness to a flat fault model. We counterbalance the consequent 3D roughness drag by increasing initial shear traction by $\tau_{drag}{}^{3D}$ (Equation 2), calculated using the spatially variable slip amplitude Δ of the reference model. We explored an alternative model (not presented here), with constant Δ equal to the peak slip of the reference model (1.14 m). It generates a higher average $\tau_{drag}{}^{3D}$ of about 3.3 MPa (cf. 1.4 MPa, Section 2.2). It may be possible to identify alternative satisfying models based on constant Δ. Nevertheless, the here presented approach of constraining Δ by the spatially variable reference fault slip appears superior due to its simpler and better constrained parametrization.

Our proposed approach to enhance smooth slip models for broadband dynamic-rupture simulations is independent of the data and generation process of the starting smooth source model. Besides the dynamic source inversion used here, kinematic slip models can serve as a reference model as well (e.g., Ma et al., 2008). However, the choices required for conversion in the latter approach may lead to several families of plausible dynamic rupture scenarios that need additional (e.g., geological) constraints to be distinguished (Tinti et al., 2021).

Although our rough fault model with topography improves the waveform fit at high frequencies, some synthetics still underestimate the observations. Additionally, a good fit of shape, duration and amplitude characteristics of broadband velocity waveforms up to 5 Hz, does not necessarily translate in capturing broadband acceleration amplitudes equally well, a challenge identified in kinematic source modeling as well (e.g., Irikura & Miyake, 2021). More complete matching of the observed records at periods <2 s may in future be enabled by: (a) considering smaller length scales (λ_{min}) of fault surface roughness, potentially further increasing high-frequency radiation at the cost of increased computational demands; (b) incorporating larger-scale non-planar fault geometry such as a listric fault geometry which has been, for instance, suggested from satellite data (Tung & Masterlark, 2018) and which may modulate peak ground velocities as a consequence of curvature focusing effect (Passone & Mai, 2017); (c) probing and quantifying the variability of the predicted shaking using alternative models from the Bayesian ensemble of the dynamic rupture inversion, (d) incorporating a more realistic Earth model to capture path

and local site conditions, that is, 3D velocity models, small-scale scattering media (Bydlon & Dunham, 2015; Imperatori & Mai, 2013), site corrections (Rodgers et al., 2020) or non-linear soil effects (Roten et al., 2012) and (e) off-fault damage (e.g., Okubo et al., 2019; Yamashita, 2000). In particular, low-velocity sedimentary basins (Lee et al., 2009; Pischiutta et al., 2021) can significantly amplify the amplitude and duration of ground motions, which may lead to improved synthetics for stations with strong site-effects, for example, CLF with site-class D (Table S1 in Supporting Information S1). However, accounting for these mechanisms in sufficient detail (at scales down to ∼100 m or less) in observationally constrained 3D broadband dynamic rupture models pose additional computational and observational challenges and their relevance for matching real earthquake recordings remains open to debate.

5. Conclusions

We present a novel approach for broadband dynamic rupture modeling constrained from low-frequency data toward generating physics-based, non-ergodic ground motion synthetics validated by observations. We generate broadband dynamic rupture models of the 2016 M_w 6.2 Amatrice earthquake by combining large-scale heterogeneous stress and frictional parameters, inferred from the best-fitting model of a Bayesian dynamic rupture inversion, with small-scale self-similar fault roughness and frictional (slip weakening distance) heterogeneity, topography, and viscoelastic seismic attenuation. We empirically quantify the 3D roughness drag governing rupture dynamics on small scales by counterbalancing its effective dynamic stress perturbations. We obtain dynamic rupture scenarios that successfully reproduce the low-frequency (<1 Hz) source characteristics of the inverted dynamic model. The combined small-scale heterogeneities of the fault geometry, frictional strength and loading enhance high-frequency source radiation. Topography elongates the synthetic waveforms by enhancing coda effects. In combination, we obtain more realistic high-frequency (up to ∼5 Hz) synthetics comparable with observed strong motion records. Our work demonstrates 3D physics-based, broadband earthquake ground-motion simulations that are tightly constrained by data-driven dynamic earthquake source inversion and allows us to quantify the first-order role of large- and small-scale dynamic source heterogeneities in the broadband seismic wavefield. Challenging future developments may focus on including 3D and site-specific wave propagation effects toward realistic fully physics-based acceleration synthetics suitable for engineering applications.

Data Availability Statement

We use the open-source software package SeisSol, available at https://github.com/SeisSol/SeisSol, branch "Norcia_sequence", commit 181fc85d5c405a8c44fe21869fe736ab1f0206d5. Input files required to run broadband dynamic rupture simulations can be downloaded from https://zenodo.org/record/7194965. The reference dynamic rupture model parameters from the Bayesian inversion are available at https://github.com/fgallovic/fd3d_tsn_pt/tree/master/example/20160824-Amatrice. The topography data from the Shuttle Radar Topography Mission (SRTM) is retrieved using the SRTM.py python package (https://github.com/tkrajina/srtm.py). Observed strong ground motion waveforms recorded by the Rete Accelerometrica Nazionale (RAN) and the Rete Sismometrica Nazionale, operated by the Italian Department of Civil Protection (DPC) and the Istituto Nazionale di Geofisica e Vulcanologia (INGV) were downloaded from the Engineering Strong-Motion database (https://esm.mi.ingv.it/, Luzi et al., 2016; Lanzano et al., 2021).

Acknowledgments
We thank Eric Dunham for helpful discussions on Text S2 in Supporting Information S1. We thank the Associate Editor Germán Prieto and two anonymous reviewers for their constructive suggestions. The work presented in this paper was supported by funding from the German Research Foundation (DFG, GA 2465/2-1). TT, AAG and TU acknowledge additional funding from the European Union's Horizon 2020 research and innovation programme (TEAR ERC Starting Grant 852992; ChEESE, grant agreement No. 823844; DT-Geo, grant agreement No. 101058129; Geo-Inquire, grant agreement No. 101058518), DFG (GA 2465/3-1), NSF (EAR-2121666) and SCEC (awards 20046, 21010). The authors acknowledge the Gauss Centre for Supercomputing e.V. (www.gauss-centre.eu, project pr63qo) for funding this project by providing computing time on the GCS Supercomputer SuperMUC-NG at Leibniz Supercomputing Centre (www.lrz.de), and King Abdullah University of Science and Technology (KAUST) Supercomputing Laboratory (www.hpc.kaust.edu.sa) for computing time on Shaheen II (project k1343).

References

Ameri, G., Gallovič, F., & Pacor, F. (2012). Complexity of the M_w 6.3 2009 L'Aquila (Central Italy) earthquake: 2. Broadband strong motion modeling. *Journal of Geophysical Research*, *117*(B4), 4308. https://doi.org/10.1029/2011JB008729

Ascione, A., Mazzoli, S., Petrosino, P., & Valente, E. (2013). A decoupled kinematic model for active normal faults: Insights from the 1980, M_S = 6.9 Irpinia earthquake, southern Italy. *The Geological Society of America Bulletin*, *125*(7–8), 1239–1259. https://doi.org/10.1130/B30814.1

Bruhat, L., Klinger, Y., Vallage, A., & Dunham, E. M. (2020). Influence of fault roughness on surface displacement: From numerical simulations to coseismic slip distributions. *Geophysical Journal International*, *220*(3), 1857–1877. https://doi.org/10.1093/gji/ggz545

Burjánek, J., & Zahradník, J. (2007). Dynamic stress field of a kinematic earthquake source model with k-squared slip distribution. *Geophysical Journal International*, *171*(3), 1082–1097. https://doi.org/10.1111/j.1365-246X.2007.03548.x

Bydlon, S. A., & Dunham, E. M. (2015). Rupture dynamics and ground motions from earthquakes in 2-D heterogeneous media. *Geophysical Research Letters*, *42*(6), 1701–1709. https://doi.org/10.1002/2014GL062982

Cheloni, D., De Novellis, V., Albano, M., Antonioli, A., Anzidei, M., Atzori, S., et al. (2017). Geodetic model of the 2016 Central Italy earthquake sequence inferred from InSAR and GPS data. *Geophysical Research Letters*, *44*(13), 6778–6787. https://doi.org/10.1002/2017GL073580

Chiaraluce, L., Di Stefano, R., Tinti, E., Scognamiglio, L., Michele, M., Casarotti, E., et al. (2017). The 2016 central Italy seismic sequence: A first look at the mainshocks, aftershocks, and source models. *Seismological Research Letters*, *88*(3), 757–771. https://doi.org/10.1785/0220160221

Cirella, A., Pezzo, G., & Piatanesi, A. (2018). Rupture kinematics and structural-rheological control of the 2016 M_w 6.1 Amatrice (Central Italy) earthquake from joint inversion of seismic and geodetic data. *Geophysical Research Letters*, *45*(22), 12302–12311. https://doi.org/10.1029/2018GL080894

Dunham, E. M., Belanger, D., Cong, L., & Kozdon, J. E. (2011). Earthquake ruptures with strongly rate-weakening friction and off-fault plasticity, part 2: Nonplanar faults. *Bulletin of the Seismological Society of America*, *101*(5), 2308–2322. https://doi.org/10.1785/0120100076

Fang, Z., & Dunham, E. M. (2013). Additional shear resistance from fault roughness and stress levels on geometrically complex faults. *Journal of Geophysical Research: Solid Earth*, *118*(7), 3642–3654. https://doi.org/10.1002/jgrb.50262

Farr, T. G., Rosen, P. A., Caro, E., Crippen, R., Duren, R., Hensley, S., et al. (2007). The shuttle radar topography mission. *Reviews of Geophysics*, *45*(2), RG2004. https://doi.org/10.1029/2005RG000183

Frankel, A., Wirth, E., Marafi, N., Vidale, J., & Stephenson, W. (2018). Broadband synthetic seismograms for magnitude 9 earthquakes on the Cascadia megathrust based on 3D simulations and stochastic synthetics, part 1: Methodology and overall results. *Bulletin of the Seismological Society of America*, *108*(5A), 2347–2369. https://doi.org/10.1785/0120180034

Galadini, F., Galli, P., & M. Moro (2003). Paleoseismology of silent faults in the Central Apennines (Italy): The Mt. Vettore and Laga Mts. faults. *Annals of Geophysics*, *46*(5), 815. https://doi.org/10.4401/ag-3456

Gallovič, F., & Ampuero, J.-P. (2015). A new strategy to compare inverted rupture models exploiting the eigenstructure of the inverse problem. *Seismological Research Letters*, *86*(6), 1679–1689. https://doi.org/10.1785/0220150096

Gallovič, F., Valentová, Ľ., Ampuero, J.-P., & Gabriel, A.-A. (2019a). Bayesian dynamic finite-fault inversion: 1. Method and synthetic test. *Journal of Geophysical Research: Solid Earth*, *124*(7), 6949–6969. https://doi.org/10.1029/2019JB017510

Gallovič, F., Valentová, Ľ., Ampuero, J.-P., & Gabriel, A.-A. (2019b). Bayesian dynamic finite-fault inversion: 2. Application to the 2016 M_w 6.2 Amatrice, Italy, earthquake. *Journal of Geophysical Research: Solid Earth*, *124*(7), 6970–6988. https://doi.org/10.1029/2019JB017512

Galvez, P., Petukhin, A., Irikura, K., & Somerville, P. (2020). Dynamic source model for the 2011 Tohoku earthquake in a wide period range combining slip reactivation with the short-period ground motion generation process. *Pure and Applied Geophysics*, *177*(5), 2143–2161. https://doi.org/10.1007/s00024-019-02210-7

Graves, R., Jordan, T. H., Callaghan, S., Deelman, E., Field, E., Juve, G., et al. (2011). CyberShake: A physics-based seismic hazard model for southern California. *Pure and Applied Geophysics*, *168*(3), 367–381. https://doi.org/10.1007/s00024-010-0161-6

Graves, R. W., & Pitarka, A. (2010). Broadband ground-motion simulation using a hybrid approach. *Bulletin of the Seismological Society of America*, *100*(5A), 2095–2123. https://doi.org/10.1785/0120100057

Guatteri, M., Mai, P. M., & Beroza, G. C. (2004). A pseudo-dynamic approximation to dynamic rupture models for strong ground motion prediction. *Bulletin of the Seismological Society of America*, *94*(6), 2051–2063. https://doi.org/10.1785/0120040037

Harris, R. A., Barall, M., Aagaard, B., Ma, S., Roten, D., Olsen, K., et al. (2018). A suite of exercises for verifying dynamic earthquake rupture codes. *Seismological Research Letters*, *89*(3), 1146–1162. https://doi.org/10.1785/0220170222

Hartzell, S., Ramírez-Guzmán, L., Meremonte, M., & Leeds, A. (2016). Ground motion in the presence of complex topography II: Earthquake sources and 3D simulations. *Bulletin of the Seismological Society of America*, *107*(1), 344–358. https://doi.org/10.1785/0120160159

Heinecke, A., Breuer, A., Rettenberger, S., Bader, M., Gabriel, A., Pelties, C., et al. (2014). Petascale high order dynamic rupture earthquake simulations on heterogeneous supercomputers. In *SC '14: Proceedings of the international conference for high performance computing, networking, storage and analysis* (pp. 3–14). https://doi.org/10.1109/SC.2014.6

Hu, Z., Olsen, K. B., & Day, S. M. (2022). 0–5 Hz deterministic 3-D ground motion simulations for the 2014 La Habra, California, Earthquake. *Geophysical Journal International*, *230*(3), 2162–2182. https://doi.org/10.1093/gji/ggac174

Ida, Y. (1972). Cohesive force across the tip of a longitudinal-shear crack and Griffith's specific surface energy. *Journal of Geophysical Research*, *77*(20), 3796–3805. https://doi.org/10.1029/JB077i020p03796

Iervolino, I., Galasso, C., & Cosenza, E. (2010). REXEL: Computer aided record selection for code-based seismic structural analysis. *Bulletin of Earthquake Engineering*, *8*(2), 339–362. https://doi.org/10.1007/s10518-009-9146-1

Imperatori, W., & Mai, P. M. (2013). Broad-band near-field ground motion simulations in 3-dimensional scattering media. *Geophysical Journal International*, *192*(2), 725–744. https://doi.org/10.1093/gji/ggs041

Irikura, K., & Miyake, H. (2021). Progress of strong motion prediction. In *17th world conference on earthquake engineering, Sendai, Japan—September 27th to October 2nd, 2021*.

Kheirdast, N., Ansari, A., & Custódio, S. (2021). Neuro-fuzzy kinematic finite-fault inversion: 2. Application to the M_w 6.2, August/24/2016, Amatrice earthquake. *Journal of Geophysical Research: Solid Earth*, *126*(8), e2020JB020773. https://doi.org/10.1029/2020JB020773

Konno, K., & Ohmachi, T. (1998). Ground-motion characteristics estimated from spectral ratio between horizontal and vertical components of microtremor. *Bulletin of the Seismological Society of America*, *88*(1), 228–241. https://doi.org/10.1785/bssa0880010228

Lanzano, G., Luzi, L., Cauzzi, C., Bienkowski, J., Bindi, D., Clinton, J., et al. (2021). Accessing European strong-motion data: An update on ORFEUS coordinated services. *Seismological Research Letters*, *92*(3), 1642–1658. https://doi.org/10.1785/0220200398

Lee, S.-J., Komatitsch, D., Huang, B.-S., & Tromp, J. (2009). Effects of topography on seismic-wave propagation: An example from northern Taiwan. *Bulletin of the Seismological Society of America*, *99*(1), 314–325. https://doi.org/10.1785/0120080020

Luzi, L., Puglia, R., Russo, E., D'Amico, M., Felicetta, C., Pacor, F., et al. (2016). The engineering strong-motion database: A platform to access Pan-European accelerometric data. *Seismological Research Letters*, *87*(4), 987–997. https://doi.org/10.1785/0220150278

Ma, S., Custodio, S., Archuleta, R. J., & Liu, P. (2008). Dynamic modeling of the 2004 M_w 6.0 Parkfield, California, earthquake. *Journal of Geophysical Research*, *113*(B2), B02301. https://doi.org/10.1029/2007jb005216

Madariaga, R. (1977). High-frequency radiation from crack (stress drop) models of earthquake faulting. *Geophysical Journal International*, *51*(3), 625–651. https://doi.org/10.1111/j.1365-246X.1977.tb04211.x

Mai, P. M., Imperatori, W., & Olsen, K. B. (2010). Hybrid broadband ground-motion simulations: Combining long-period deterministic synthetics with high-frequency multiple S-to-S backscattering hybrid broadband ground-motion simulations: Combining deterministic synthetics with backscattering. *Bulletin of the Seismological Society of America*, *100*(5A), 2124–2142. https://doi.org/10.1785/0120080194

Mai, P. M., Schorlemmer, D., Page, M., Ampuero, J., Asano, K., Causse, M., et al. (2016). The earthquake-source inversion validation (SIV) project. *Seismological Research Letters*, *87*(3), 690–708. https://doi.org/10.1785/0220150231

Michele, M., Chiaraluce, L., Di Stefano, R., & Waldhauser, F. (2020). Fine-scale structure of the 2016–2017 central Italy seismic sequence from data recorded at the Italian National Network. *Journal of Geophysical Research: Solid Earth*, *125*(4), e2019JB018440. https://doi.org/10.1029/2019JB018440

Michele, M., Di Stefano, R., Chiaraluce, L., Cattaneo, M., De Gori, P., Monachesi, G., et al. (2016). The Amatrice 2016 seismic sequence: A preliminary look at the mainshock and aftershocks distribution. *Annals of Geophysics*, *59*, 1–8. https://doi.org/10.4401/ag-7227

Moschetti, M. P., Hartzell, S., Ramírez-Guzmán, L., Frankel, A. D., Angster, S. J., & Stephenson, W. J. (2017). 3D ground-motion simulations of M_w 7 earthquakes on the salt lake city segment of the Wasatch fault zone: Variability of long-period ($T \geq 1$) ground motions and sensitivity to kinematic rupture parameters. *Bulletin of the Seismological Society of America*, *107*(4), 1704–1723. https://doi.org/10.1785/0120160307

Okubo, K., Bhat, H. S., Rougier, E., Marty, S., Schubnel, A., Lei, Z., et al. (2019). Dynamics, radiation, and overall energy budget of earthquake rupture with coseismic off-fault damage. *Journal of Geophysical Research: Solid Earth*, *124*(11), 11771–11801. https://doi.org/10.1029/2019JB017304

Olsen, K. B., & Mayhew, J. E. (2010). Goodness-of-fit criteria for broadband synthetic seismograms, with application to the 2008 M_w 5.4 Chino Hills, California, earthquake. *Seismological Research Letters*, *81*(5), 715–723. https://doi.org/10.1785/gssrl.81.5.715

Palmer, A. C., Rice, J. R., & Hill, R. (1973). The growth of slip surfaces in the progressive failure of over-consolidated clay. *Proceedings of the Royal Society of London A. Mathematical and Physical Sciences*, *332*(1591), 527–548. https://doi.org/10.1098/rspa.1973.0040

Passone, L., & Mai, P. M. (2017). Kinematic earthquake ground-motion simulations on listric normal faults. *Bulletin of the Seismological Society of America*, *107*(6), 2980–2993. https://doi.org/10.1785/0120170111

Petersen, M. D., Shumway, A. M., Powers, P. M., Mueller, C. S., Moschetti, M. P., Frankel, A. D., et al. (2019). The 2018 update of the US national seismic hazard model: Overview of model and implications. *Earthquake Spectra*, *36*(1), 5–41. https://doi.org/10.1177/8755293019878199

Peyrat, S., & Olsen, K. B. (2004). Nonlinear dynamic rupture inversion of the 2000 Western Tottori, Japan, earthquake. *Geophysical Research Letters*, *31*(5), 2004. https://doi.org/10.1029/2003GL019058

Pischiutta, M., Akinci, A., Tinti, E., & Herrero, A. (2021). Broad-band ground-motion simulation of 2016 Amatrice earthquake, Central Italy. *Geophysical Journal International*, *224*(3), 1753–1779. https://doi.org/10.1093/gji/ggaa412

Pitarka, A., Akinci, A., De Gori, P., & Buttinelli, M. (2021). Deterministic 3D ground-motion simulations (0–5 Hz) and surface topography effects of the 30 October 2016 M_w 6.5 Norcia, Italy, earthquake. *Bulletin of the Seismological Society of America*, *112*(1), 262–286. https://doi.org/10.1785/0120210133

Pizzi, A., Di Domenica, A., Gallovič, F., Luzi, L., & Puglia, R. (2017). Fault segmentation as constraint to the occurrence of the Main shocks of the 2016 Central Italy seismic sequence. *Tectonics*, *36*(11), 2370–2387. https://doi.org/10.1002/2017TC004652

Power, W. L., & Tullis, T. E. (1991). Euclidean and fractal models for the description of rock surface roughness. *Journal of Geophysical Research*, *96*(B1), 415–424. https://doi.org/10.1029/90JB02107

Premus, J., Gallovič, F., Hanyk, L., & Gabriel, A. (2020). FD3D_TSN: A fast and simple code for dynamic rupture simulations with GPU acceleration. *Seismological Research Letters*, *91*(5), 2881–2889. https://doi.org/10.1785/0220190374

Ragon, T., Sladen, A., & Simons, M. (2018). Accounting for uncertain fault geometry in earthquake source inversions—I: Theory and simplified application. *Geophysical Journal International*, *214*(2), 1174–1190. https://doi.org/10.1093/gji/ggy187

Ripperger, J., Mai, P. M., & Ampuero, J.-P. (2008). Variability of near-field ground motion from dynamic earthquake rupture simulations. *Bulletin of the Seismological Society of America*, *98*(3), 1207–1228. https://doi.org/10.1785/0120070076

Rodgers, A. J., Pitarka, A., Pankajakshan, R., Sjögreen, B., & Petersson, N. A. (2020). Regional-scale 3D ground-motion simulations of M_w 7 earthquakes on the Hayward fault, northern California resolving frequencies 0–10 Hz and including site-response corrections. *Bulletin of the Seismological Society of America*, *110*(6), 2862–2881. https://doi.org/10.1785/0120200147

Roten, D., Olsen, K. B., Day, S. M., Cui, Y., & Fäh, D. (2014). Expected seismic shaking in Los Angeles reduced by San Andreas fault zone plasticity. *Geophysical Research Letters*, *41*(8), 2769–2777. https://doi.org/10.1002/2014GL059411

Roten, D., Olsen, K. B., & Pechmann, J. C. (2012). 3D simulations of *M*7 earthquakes on the Wasatch Fault, Utah, Part II: Broadband (0–10 Hz) ground motions and nonlinear soil behavior. *Bulletin of the Seismological Society of America*, *102*(5), 2008–2030. https://doi.org/10.1785/0120110286

Sambridge, M. (2013). A parallel tempering algorithm for probabilistic sampling and multimodal optimization. *Geophysical Journal International*, *196*(1), 357–374. https://doi.org/10.1093/gji/ggt342

Savran, W. H., & Olsen, K. B. (2020). Kinematic rupture generator based on 3-D spontaneous rupture simulations along geometrically rough faults. *Journal of Geophysical Research: Solid Earth*, *125*(10), e2020JB019464. https://doi.org/10.1029/2020JB019464

Schmedes, J., Archuleta, R. J., & Lavallée, D. (2010). Correlation of earthquake source parameters inferred from dynamic rupture simulations. *Journal of Geophysical Research*, *115*(B3), B03304. https://doi.org/10.1029/2009JB006689

Shi, Z., & Day, S. M. (2013). Rupture dynamics and ground motion from 3-D rough-fault simulations. *Journal of Geophysical Research: Solid Earth*, *118*(3), 1122–1141. https://doi.org/10.1002/jgrb.50094

Shimizu, K., Yagi, Y., Okuwaki, R., & Fukahata, Y. (2020). Development of an inversion method to extract information on fault geometry from teleseismic data. *Geophysical Journal International*, *220*(2), 1055–1065. https://doi.org/10.1093/gji/ggz496

Somerville, P., Irikura, K., Graves, R., Sawada, S., Wald, D., Abrahamson, N., et al. (1999). Characterizing earthquake slip models for the prediction of strong ground motion. *Seismological Research Letters*, *70*(1), 59–80. https://doi.org/10.1785/gssrl.70.1.59

Takemura, S., Furumura, T., & Maeda, T. (2015). Scattering of high-frequency seismic waves caused by irregular surface topography and small-scale velocity inhomogeneity. *Geophysical Journal International*, *201*(1), 459–474. https://doi.org/10.1093/gji/ggv038

Tinti, E., Casarotti, E., Ulrich, T., Taufiqurrahman, T., Li, D., & Gabriel, A.-A. (2021). Constraining families of dynamic models using geological, geodetic and strong ground motion data: The M_w 6.5, October 30th, 2016, Norcia earthquake, Italy. *Earth and Planetary Science Letters*, *576*, 117237. https://doi.org/10.1016/j.epsl.2021.117237

Tinti, E., Fukuyama, E., Piatanesi, A., & Cocco, M. (2005). A kinematic source-time function compatible with earthquake dynamics. *Bulletin of the Seismological Society of America*, *95*(4), 1211–1223. https://doi.org/10.1785/0120040177

Tinti, E., Scognamiglio, L., Michelini, A., & Cocco, M. (2016). Slip heterogeneity and directivity of the M_L 6.0, 2016, Amatrice earthquake estimated with rapid finite-fault inversion. *Geophysical Research Letters*, *43*(20), 10745–10752. https://doi.org/10.1002/2016GL071263

Tondi, E., Jablonská, D., Volatili, T., Michele, M., Mazzoli, S., & Pierantoni, P. P. (2020). The Campotosto linkage fault zone between the 2009 and 2016 seismic sequences of central Italy: Implications for seismic hazard analysis. *GSA Bulletin*, *133*(7–8), 1679–1694. https://doi.org/10.1130/B35788.1

Tung, S., & Masterlark, T. (2018). Resolving source geometry of the 24 August 2016 Amatrice, Central Italy, earthquake from InSAR data and 3D finite-element modeling. *Bulletin of the Seismological Society of America*, *108*(2), 553–572. https://doi.org/10.1785/0120170139

Valentová, Ľ., Gallovič, F., & Hok, S. (2021). Near-source ground motions and their variability derived from dynamic rupture simulations constrained by NGA-West2 GMPEs. *Bulletin of the Seismological Society of America*, *111*(5), 2559–2573. https://doi.org/10.1785/0120210073

Walters, R. J., Gregory, L. C., Wedmore, L. N. J., Craig, T. J., McCaffrey, K., Wilkinson, M., et al. (2018). Dual control of fault intersections on stop-start rupture in the 2016 Central Italy seismic sequence. *Earth and Planetary Science Letters*, *500*, 1–14. https://doi.org/10.1016/j.epsl.2018.07.043

Wirth, E. A., Frankel, A. D., Marafi, N., Vidale, J. E., & Stephenson, W. J. (2018). Broadband synthetic seismograms for magnitude 9 earthquakes on the Cascadia megathrust based on 3D simulations and stochastic synthetics, Part 2: Rupture parameters and variability. *Bulletin of the Seismological Society of America*, *108*(5A), 2370–2388. https://doi.org/10.1785/0120180029

Withers, K. B., Moschetti, M. P., & Thompson, E. M. (2020). A machine learning approach to developing ground motion models from simulated ground motions. *Geophysical Research Letters*, *47*(6), e2019GL086690. https://doi.org/10.1029/2019GL086690

Withers, K. B., Olsen, K. B., Day, S. M., & Shi, Z. (2018). Ground motion and intra-event variability from 3D deterministic broadband (0–7.5 Hz) simulations along a nonplanar strike-slip fault. *Bulletin of the Seismological Society of America*, *109*(1), 229–250. https://doi.org/10.1785/0120180006

Wollherr, S., Gabriel, A. A., & Mai, P. M. (2019). Landers 1992 "reloaded": Integrative dynamic earthquake rupture modeling. *Journal of Geophysical Research: Solid Earth*, *124*(7), 6666–6702. https://doi.org/10.1029/2018JB016355

Yamashita, T. (2000). Generation of microcracks by dynamic shear rupture and its effects on rupture growth and elastic wave radiation. *Geophysical Journal International*, *143*(2), 395–406. https://doi.org/10.1046/j.1365-246X.2000.01238.x

References From the Supporting Information

Aochi, H., & Madariaga, R. (2003). The 1999 İzmit, Turkey earthquake: Nonplanar fault structure, dynamic rupture process, and strong ground motion. *Bulletin of the Seismological Society of America*, *93*(3), 1249–1266. https://doi.org/10.1785/0120020167

Day, S. M., Dalguer, L. A., Lapusta, N., & Liu, Y. (2005). Comparison of finite difference and boundary integral solutions to three-dimensional spontaneous rupture. *Journal of Geophysical Research*, *110*(B12), B12307. https://doi.org/10.1029/2005JB003813

Dumbser, M., & Käser, M. (2006). An arbitrary high-order discontinuous Galerkin method for elastic waves on unstructured meshes—II. The three-dimensional isotropic case. *Geophysical Journal International*, *167*(1), 319–336. https://doi.org/10.1111/j.1365-246X.2006.03120.x

Duru, K., & Dunham, E. M. (2016). Dynamic earthquake rupture simulations on non-planar faults embedded in 3D geometrically complex, heterogeneous elastic solids. *Journal of Computational Physics*, *305*, 185–207. https://doi.org/10.1016/j.jcp.2015.10.021

Eurocode 8 (EC8). (2004). *EN 1998-1: Design of structures for earthquake resistance, part 1: General rules, seismic actions and rules for buildings*. European Committee for Standardization (CEN).

Käser, M., Hermann, V., & de la Puente, J. (2008). Quantitative accuracy analysis of the discontinuous Galerkin method for seismic wave propagation. *Geophysical Journal International*, *173*(3), 990–999. https://doi.org/10.1111/j.1365-246X.2008.03781.x

Pelties, C., de la Puente, J., Ampuero, J.-P., Brietzke, G. B., & Käser, M. (2012). Three-dimensional dynamic rupture simulation with a high-order discontinuous Galerkin method on unstructured tetrahedral meshes. *Journal of Geophysical Research*, *117*(B2), B02309. https://doi.org/10.1029/2011JB008857

Pelties, C., Gabriel, A.-A., & Ampuero, J.-P. (2014). Verification of an ADER-DG method for complex dynamic rupture problems. *Geoscientific Model Development*, *7*(3), 847–866. https://doi.org/10.5194/gmd-7-847-2014

Simmetrix Inc. (2017). SimModeler: Simulation modeling suite 11.0 documentation. Retrieved from www.simmetrix.org

Wollherr, S., Gabriel, A.-A., & Uphoff, C. (2018). Off-fault plasticity in three-dimensional dynamic rupture simulations using a modal discontinuous Galerkin method on unstructured meshes: Implementation, verification and application. *Geophysical Journal International*, *214*(3), 1556–1584. https://doi.org/10.1093/gji/ggy213